Nonlinear dynamics of island coarsening and stabilization during strained film heteroepitaxy

Champika G. Gamage and Zhi-Feng Huang

Department of Physics and Astronomy, Wayne State University, Detroit, Michigan 48201, USA

Nonlinear evolution of three-dimensional strained islands or quantum dots in heteroepitaxial thin films is studied via a continuum elasticity model and both perturbation analysis of the system and numerical simulations of the corresponding nonlinear dynamic equation governing the film morphological profile. Three regimes of island array evolution are identified and examined, including a film instability regime at early stage, a nonlinear coarsening regime at intermediate times, and the crossover to a saturated asymptotic state, with detailed behavior depending on film-substrate misfit strains but not qualitatively on finite system sizes. The phenomenon of island array stabilization, which corresponds to the formation of steady but nonordered arrays of strained quantum dots, occurs at later time for smaller misfit strain. It is found to be controlled by the strength of film-substrate wetting interaction which would constrain the valley-to-peak mass transport and hence the growth of island height, and also determined by the effect of elastic interaction between surface islands and the high-order strain energy of individual islands at late evolution stage. The results are compared to previous experimental and theoretical studies on quantum dot coarsening and stabilization.

I. INTRODUCTION

The formation of surface nanostructures such as islands or quantum dots during heteroepitaxy of strained films has attracted continuing great interest due to its importance in both fundamental understanding of material growth and its wide range of applications particularly for optoelectronic nanodevices [1–3]. One of the underlying mechanisms of island formation has been attributed to the occurrence of morphological instability of the strained film (i.e., the Asaro-Tiller-Grinfeld instability [4]), for which the competition between the stabilization effect of film surface energy and the destabilization effect of system elastic energy due to film-substrate misfit strain plays a key role. This involves the process of stress release in the film via surface mass transport driven by local energy gradient and consequently the formation of coherent nonplanar surface structures such as nanoscale islands [5,6]. Compared to other formation mechanisms such as thermally activated nucleation, a main feature here is the continuous, nucleationless nature of the film instability and the subsequent island growth that starts from rough surface [7–9]. It results in more regular and correlated arrays of self-assembled quantum dots that are appealing for a variety of applications.

The onset of this type of quantum dots or strained islands formation has been well understood, as studied via detailed instability analysis for both single-component [5,6] and alloy strained films [10–13] as well as multilayers or superlattices [14,15]. Such film instability, showing as surface ripples and cell-like undulations which are the precursor of coherent island formation, has been observed in experiments of semiconductor heteroepitaxial films such as SiGe [7,8]. On the other hand, the subsequent nonlinear evolution of these strained dots, which are well beyond the initial linear stability stage, is more complicated and much less understood. A typical phenomenon is the coarsening of quantum dot islands, showing as the increase of average island size during film evolution and the shrinking of small dots. Such scenario has been observed in experiments of Ge/Si(001) [16–19], SiGe/Si(001) [20], and

InAs/GaAs(001) [21], although with different mechanisms and behavior of coarsening reported. For the example of Ge-Si systems that have been extensively studied, nonlinear island coarsening rate that deviates from classical results of Ostwald ripening has been found; however, it was associated with different mechanisms of island morphology evolution in different experiments, such as the effect of island shape transition accompanying the coarsening process [16–18] or a contrasting kinetic picture that incorporates elastic interactions but not island shape transition [20]. Also, the slowing [16] or suppression [19] of coarsening process at late stage and the resulting stabilized quantum dot arrays have been observed in some experiments of growing [16,22] and post-deposition [17,19] films, but not in others [20].

The corresponding theoretical or computational study on nonlinear island evolution is also far from conclusive. Most efforts are based on continuum approaches including continuum elasticity theory [23–35] and phase field methods [36,37], in addition to other modeling techniques that incorporate crystalline details, such as kinetic Monte Carlo method with elastic interaction [38–40] and the recently developed phase-field-crystal (PFC) model and the associated amplitude equation formalism [41–44]. For continuum elasticity modeling, which is the current main avenue for studying strained island coarsening due to the large length and time scales involved, much recent focus has been put on the derivation and simulation of nonlinear evolution equations through approximating the system elasticity and the dynamics of film morphology via perturbation methods. Two limits of system configuration were addressed in early studies of such approach, including the limit of perfectly rigid substrate [24,30] and the case of infinitely thick strained film [28]. More recently, similar approximation has been applied to heteroepitaxial systems consisting of a strained thin film grown on an elastic substrate as configured in most experiments. The corresponding reduced nonlinear evolution equations have been derived and simulated, based on different approximations. In the long-wave or small-slope approximation of film surface profile [31,34,35], much larger

variation length scale along the film surface was assumed as compared to that of the film normal, while other studies were based on the expansion of system stress in terms of small gradient of the film surface height [33]. Some physical mechanisms in thin film growth have also been incorporated, such as the wetting effect between the strained film and the underlying substrate. These approaches are more efficient for large scale simulations, as compared to directly solving the full system elasticity problem and the corresponding full dynamic equation of morphological profile, which instead is of high computational cost and hence usually involves limited system size, island number, and evolution time particularly for three-dimensional (3D) systems.

Despite the success of these theoretical approaches in describing properties of quantum dot formation and film morphology, some behavior of film nonlinear evolution, particularly the process of island coarsening versus stabilization, is still not well understood, with inconsistent results given in different studies [26,29,32–35,45]. For the case of post-deposition film as examined in most simulations, coarsening of strained island arrays has been reproduced, although with different coarsening rate found in different approaches [29,34,35]. One of the main differences in these works is the result for asymptotic and steady state of the film morphology. Stable arrays of quantum dots that persist after the coarsening stage have been obtained in both studies of the reduced nonlinear evolution equation [33,45] and the direct solution of the full elasticity problem [26,32], consistent with the observation in some Si-Ge experiments [17,19]. However, as in some other experiments [20], such scenario of the suppression or cessation of island coarsening was not found in other modeling processes [29,34], and recent nonlinear analysis of a system evolution equation suggested that a regular quantum dot array would be unstable as a result of subcritical bifurcation [34]. Note that in many previous studies the saturation of island coarsening process has been attributed to the effect of surface-energy anisotropy [26,32,45], although the phenomenon of island stabilization has also been observed in recent simulation without such anisotropy effect [33]. These discrepancies in modeling results could probably be related to different types of approximation and various ways of small variable expansion and truncation involved in different approaches, and/or the difficulty in simulating large enough system size and long enough evolution time required for experimental comparison.

In this paper, we focus on the nonlinear evolution of strained quantum dot islands grown epitaxially on an elastic substrate, based on a continuum elasticity model and the development of a systematic approach for approximately solving the film-substrate elastic state via a perturbation analysis in Fourier space. Results up to second-order perturbation of surface morphology are presented, and our approach can be readily extended to incorporate higher-order elastic solutions. We can then derive a new nonlinear evolution equation governing the dynamics of strained film morphology, which allows us to systematically examine the detailed behavior of film evolution at large enough spatial and temporal scales. This nonlinear equation, with the incorporation of the wetting effect, is applied to the study of island coarsening and stabilization process in post-deposition films. Our focus is on systems of small misfit strains, which correspond to large enough length scale of the resulting surface structure as compared to the scale of crystalline lattice. (This is based on recent studies [42] showing that continuum approaches, such as the continuum elasticity theory developed here, can well describe the films in weak strain limit, but not for large misfit stress, which would lead to qualitatively different behavior of surface islands due to the effects of discrete lattice structure.) The whole sequence of island evolution can be reproduced in our numerical simulations, including three characteristic regimes: the development of morphological instability and island formation at early times, nonlinear coarsening of islands at intermediate stage, and the slowing of such coarsening process which leads to a saturated state of steady quantum dot arrays. We also investigate the mechanisms underlying the phenomenon of island stabilization, based on the study of wetting effect on the constraint of surface mass transport between island valleys and peaks, and also on a detailed examination of strain relaxation process via studying the temporal evolution and spatial distribution of elastic energy density at the film surface. We identify a factor responsible for suppressing the island growth and coarsening, which is attributed to the effect of high-order elastic energy of individual islands and the elastic interaction between them.

II. MODEL

Assume that a strained film of spatially varying height $h(x,y,t)$ is deposited epitaxially on a semi-infinite elastic substrate that occupies the region $z < 0$. The misfit strain in the film with respect to the substrate is given by $\epsilon_m = (a_f - a_s)/a_s$, where a_f and a_s are the lattice spacings of the film and the substrate, respectively. For such coherent, dislocation-free system, the evolution of the film surface morphological profile $h(x,y,t)$ is governed by

$$\frac{\partial h}{\partial t} = \Gamma_h \sqrt{g} \nabla_s^2 \frac{\delta \mathcal{F}}{\delta h} + v, \qquad (1)$$

where Γ_h is the kinetic coefficient determined by surface diffusion, ∇_s^2 is the surface Laplacian, v is the deposition rate (with $v = 0$ for the post-deposition case), and $g = 1 + |\nabla h|^2$. Here, the effect of film-substrate interdiffusion is neglected. The total free energy functional $\mathcal{F}$ consists of two parts, including the elastic energy $\mathcal{F}_{el} = \int_{-\infty}^{h} d^3r \, \mathcal{E}$ where $\mathcal{E}$ represents the strain energy density, and the surface free energy $\mathcal{F}_s = \int d^2r \, \gamma_s(h)\sqrt{g}$ where γ_s is the thickness-dependent, isotropic surface tension with the effect of wetting interaction between the film and substrate incorporated. The dynamic equation (1) can then be rewritten as [6,31,34]

$$\frac{\partial h}{\partial t} = \Gamma_h \sqrt{g} \nabla_s^2 [\gamma \kappa + W(h) + \mathcal{E}^f] + v, \qquad (2)$$

where κ is the mean surface curvature, γ is the surface-energy density, $\mathcal{E}^f$ gives the film elastic energy density at the surface $z = h$, and the wetting potential W can be approximated via a phenomenological glued-layer wetting model [34]

$$W(h) = -w \left(\frac{h}{h_{ml}} \right)^{-\alpha_w} e^{-h/h_{ml}}. \qquad (3)$$

Here, w gives the strength of the film-substrate wetting interaction, h_{ml} is the characteristic wetting-layer thickness

that is usually of a few monolayers, and the exponent α_w (>0) gives the singularity of the potential W in the limit of $h \to 0$ that emulates the persistence of the wetting layer during film evolution [34].

The formulation of elasticity for this film-substrate system has been well established [6]. In isotropic, linear elasticity theory (i.e., with harmonic approximation), the elastic energy density is given by $\mathcal{E} = \frac{1}{2}\sigma_{ij}u_{ij}$, where $i,j = x,y,z$, and u_{ij} is the linear elastic strain tensor defined by $u_{ij} = (\partial_j u_i + \partial_i u_j)/2$ (with u_i the displacement field). From Hooke's law for isotropic elastic system, the stress tensor σ_{ij} in the strained film is expressed by

$$\sigma_{ij} = 2\mu \left[\frac{\nu}{1-2\nu}\delta_{ij}u_{kk} + u_{ij} - \frac{1+\nu}{1-2\nu}\epsilon_m \delta_{ij} \right], \quad (4)$$

where μ is the shear modulus and ν is the Poisson ratio. The stress tensor in the substrate is also given by Eq. (4) with $\epsilon_m = 0$. Here, for simplicity we have assumed equal elastic constants in the film and substrate, which corresponds to the situation in most experimental systems where the difference of elastic constants between film and substrate materials is not significant.

Since the elastic relaxation occurs at a time scale of orders of magnitude faster than that of the atomic diffusion process and the associated system morphological evolution, it is usually assumed that the mechanical equilibrium condition $\partial_j \sigma_{ij} = 0$ is always satisfied in both film and substrate. Using Eq. (4), we can obtain Navier's equations in the whole film-substrate system

$$(1-2\nu)\partial_j^2 u_i + \partial_i \partial_j u_j = 0. \quad (5)$$

The corresponding boundary condition on the top film surface is given by

$$\sigma_{ij}^f n_j = 0 \quad \text{at} \quad z = h(x,y,t), \quad (6)$$

due to the neglecting of external pressure on the free surface, while the boundary conditions at the film-substrate interface is determined by the continuity of stress and displacement fields:

$$\sigma_{ij}^f n_j = \sigma_{ij}^s n_j \quad \text{and} \quad u_i^f = u_i^s \quad \text{at} \quad z = 0. \quad (7)$$

Here, n_j is the unit vector normal to the film surface or the film-substrate interface, and the subscripts "f" and "s" refer to the film and substrate phases, respectively. Also, inside the substrate region, which is far away from the film, we have

$$u_i^s, u_{ij}^s \to 0 \quad \text{for} \quad z \to -\infty. \quad (8)$$

III. PERTURBATION ANALYSIS AND NONLINEAR EVOLUTION EQUATION

To solve this elasticity problem, we adopt a perturbation analysis in Fourier space based on the expansion of system elastic quantities on the small vertical variation of film surface morphology. More specifically, given the Fourier transform of the film morphological profile

$$h = \bar{h} + \sum_q \hat{h}(\mathbf{q},t)e^{i(q_x x + q_y y)}, \quad (9)$$

where $\bar{h} = h_0 + vt$ is the average film thickness at any time t (with h_0 the initial film thickness), the Fourier components of

the displacement field $\hat{u}_i(\mathbf{q})$, stress tensor $\hat{\sigma}_{ij}(\mathbf{q})$ ($i,j = x,y,z$), and film elastic energy density $\hat{\mathcal{E}}^f$ are expanded in the order of surface perturbation $\hat{h}(\mathbf{q})$, i.e.,

$$u_i = \bar{u}_i + \sum_q \hat{u}_i(\mathbf{q})e^{i(q_x x + q_y y)}, \quad \hat{u}_i = \varepsilon \hat{u}_i^{(1)} + \varepsilon^2 \hat{u}_i^{(2)} + \cdots,$$

$$\sigma_{ij} = \bar{\sigma}_{ij} + \sum_q \hat{\sigma}_{ij}(\mathbf{q})e^{i(q_x x + q_y y)}, \quad \hat{\sigma}_{ij} = \varepsilon \hat{\sigma}_{ij}^{(1)} + \varepsilon^2 \hat{\sigma}_{ij}^{(2)} + \cdots,$$

$$\mathcal{E}^f = \bar{\mathcal{E}}^f + \sum_q \hat{\mathcal{E}}^f(\mathbf{q})e^{i(q_x x + q_y y)}, \quad \hat{\mathcal{E}}^f = \hat{\mathcal{E}}^{(1)f} + \hat{\mathcal{E}}^{(2)f} + \cdots.$$

$$(10)$$

Here, we have introduced a small parameter ε, which represents the order of surface perturbation function $\hat{h}(\mathbf{q})$; also, $\hat{\mathcal{E}}^{(\xi)f} \sim \mathcal{O}(\varepsilon^\xi)$ (with $\xi = 1,2,\ldots$) in Eq. (10). For the zeroth-order base state with planar, uniformly strained film, the elasticity solutions are given by Ref. [6]: $\bar{u}_i^f = 0$ ($i = x,y$) and $\bar{u}_z^f = \bar{u}_{zz}^f z$ for the displacement fields, the strain tensor $\bar{u}_{ij}^f = 0$ except for $\bar{u}_{zz}^f = \epsilon_m(1+\nu)/(1-\nu)$, the stress tensor $\bar{\sigma}_{ij}^f = 0$ except for $\bar{\sigma}_{xx}^f = \bar{\sigma}_{yy}^f = -2\mu\bar{u}_{zz}^f$, and the zeroth-order elastic energy density $\bar{\mathcal{E}}^f = E\epsilon_m^2/(1-\nu)$ (where E is the Young's modulus). For the substrate, the corresponding base state is stress free, with $\bar{u}_i^s = \bar{u}_{ij}^s = \bar{\sigma}_{ij}^s = 0$.

The elastic properties at higher orders can be obtained by substituting the expansions (9) and (10) into Eqs. (5)–(8). In Fourier space, Navier's equations (5) can be rewritten as

$$(1-2\nu)(\partial_z^2 - q^2)\hat{u}_j^{(\xi)} + iq_j \left[iq_x\hat{u}_x^{(\xi)} + iq_y\hat{u}_y^{(\xi)} + \partial_z\hat{u}_z^{(\xi)} \right] = 0$$
$$\text{for } j = x,y, \quad (11)$$

$$(1-2\nu)(\partial_z^2 - q^2)\hat{u}_z^{(\xi)} + \partial_z \left[iq_x\hat{u}_x^{(\xi)} + iq_y\hat{u}_y^{(\xi)} + \partial_z\hat{u}_z^{(\xi)} \right] = 0$$
$$(12)$$

for ξth-order expansion ($\xi = 1,2,\ldots$). The corresponding general solutions have the same format as that obtained in Ref. [6] for first-order equations, which read as

$$\varepsilon^\xi \hat{u}_i^{(\xi)f} = \begin{bmatrix} \alpha_x^{(\xi)} \\ \alpha_y^{(\xi)} \\ \alpha_z^{(\xi)} \end{bmatrix} \cosh(qz) + \begin{bmatrix} \beta_x^{(\xi)} \\ \beta_y^{(\xi)} \\ \beta_z^{(\xi)} \end{bmatrix} \sinh(qz)$$
$$- \begin{bmatrix} C^{(\xi)}iq_x/q \\ C^{(\xi)}iq_y/q \\ D^{(\xi)} \end{bmatrix} z\sinh(qz) - \begin{bmatrix} D^{(\xi)}iq_x/q \\ D^{(\xi)}iq_y/q \\ C^{(\xi)} \end{bmatrix}$$
$$\times z\cosh(qz) \quad (13)$$

for the film, and

$$\varepsilon^\xi \hat{u}_i^{(\xi)s} = \begin{bmatrix} \alpha_x^{(\xi)} \\ \alpha_y^{(\xi)} \\ \alpha_z^{(\xi)} \end{bmatrix} e^{qz} - \begin{bmatrix} iq_x/q \\ iq_y/q \\ 1 \end{bmatrix} B^{(\xi)}ze^{qz} \quad (14)$$

for the substrate after using the boundary conditions (7) and (8) at the film-substrate interface and inside the substrate. The coefficients $\alpha_i^{(\xi)}$, $\beta_i^{(\xi)}$, $C^{(\xi)}$, $D^{(\xi)}$, and $B^{(\xi)}$ in Eqs. (13) and (14) are determined via the expansion of boundary conditions (6) and (7) in orders of ε. Note that the first-order solution has been known with the use of linearized boundary conditions [6,10],

with the perturbed elastic energy density being given by

$$\hat{\mathcal{E}}^{(1)f} = -\frac{2E(1+\nu)}{1-\nu}\epsilon_m^2 q \hat{h}(\mathbf{q}).$$ (15)

For the second-order expansion of the boundary conditions, at the top surface of the film $z = h$, Eq. (6) can be written as

$$-\sum_{\mathbf{q}'} i(q_x - q_x')\varepsilon\hat{\sigma}_{jx}^{(1)f}(\mathbf{q}')\hat{h}(\mathbf{q}-\mathbf{q}') - \sum_{\mathbf{q}'} i(q_y - q_y')\varepsilon\hat{\sigma}_{jy}^{(1)f}(\mathbf{q}')\hat{h}(\mathbf{q}-\mathbf{q}') + \varepsilon^2\hat{\sigma}_{jz}^{(2)f}(\mathbf{q}) = 0,$$ (16)

while the continuity of stress at the film-substrate interface $z = 0$ [i.e., Eq. (7)] yields

$$\hat{\sigma}_{jz}^{(2)f}(\mathbf{q}) = \hat{\sigma}_{jz}^{(2)s}(\mathbf{q}),$$ (17)

with $j = x, y, z$. Substituting Eqs. (13) and (14) to these boundary conditions (16) and (17), the second-order coefficients of the solution can be obtained as follows:

$$q\alpha_z^{(2)} = q\beta_z^{(2)} = -e^{-q\bar{h}}\left[\frac{a_1^{(2)}q_x + b_1^{(2)}q_y}{2\mu q}(1 - 2\nu + q\bar{h}) - \frac{c_1^{(2)}}{2\mu}(2 - 2\nu + q\bar{h})\right],$$

$$iq_x\alpha_x^{(2)} + iq_y\alpha_y^{(2)} = iq_x\beta_x^{(2)} + iq_y\beta_y^{(2)} = e^{-q\bar{h}}\left[\frac{a_1^{(2)}q_x + b_1^{(2)}q_y}{2\mu q}(q\bar{h} - 2 + 2\nu) + \frac{c_1^{(2)}}{2\mu}(1 - 2\nu + q\bar{h})\right],$$ (18)

$$C^{(2)} = D^{(2)} = B^{(2)} = e^{-q\bar{h}}\left[-\frac{a_1^{(2)}q_x + b_1^{(2)}q_y}{2\mu q} + \frac{c_1^{(2)}}{2\mu}\right],$$

where

$$a_1^{(2)}q_x + b_1^{(2)}q_y = \sum_{\mathbf{q}'} \hat{h}(\mathbf{q}')\hat{h}(\mathbf{q}-\mathbf{q})\left\{\frac{2E\epsilon_m}{q'(1-\nu)}\left[q_x(q_x - q_x')(q_x'^2 + \nu q_y'^2) + q_y(q_y - q_y')(q_y'^2 + \nu q_x'^2)\right]\right.$$

$$\left. + 2E\epsilon_m\frac{q_x'q_y'}{q'}[q_x(q_y - q_y') + q_y(q_x - q_x')]\right\}$$ (19)

and

$$c_1^{(2)} = \sum_{\mathbf{q}'} \hat{h}(\mathbf{q}')\hat{h}(\mathbf{q}-\mathbf{q}')\frac{E\epsilon_m}{1-\nu}[q_x'(q_x - q_x') + q_y'(q_y - q_y')].$$ (20)

Based on the above solution, we can determine the second-order elastic energy density as

$$\hat{\mathcal{E}}^{(2)f} = \sum_{\mathbf{q}'}\left[\frac{1+\nu}{2E}\varepsilon^2\hat{\sigma}_{ij}^{(1)f}(\mathbf{q}')\hat{\sigma}_{ij}^{(1)f}(\mathbf{q}-\mathbf{q}')\right.$$

$$\left. -\frac{\nu}{2E}\varepsilon^2\hat{\sigma}_{ll}^{(1)f}(\mathbf{q}')\hat{\sigma}_{ll}^{(1)f}(\mathbf{q}-\mathbf{q}')\right]$$

$$+ \frac{E\epsilon_m}{1-\nu}\left[(1-\nu)\frac{a_1^{(2)}q_x + b_1^{(2)}q_y}{\mu q} - (1-2\nu)\frac{c_1^{(2)}}{2\mu}\right],$$ (21)

where the expressions of first-order stress tensor $\hat{\sigma}_{ij}^{(1)f}$ at the top surface are given in the Appendix [see Eq. (A1)]. The second-order stress tensor can also be calculated, with results shown in Eqs. (A2)–(A7).

We then derive the nonlinear evolution equation for film surface morphology from Eq. (2), using the results of perturbed elastic energy density given in Eqs. (15) and (21). All the terms in the dynamic equation (2) are expanded up to second order of surface perturbation $\hat{h}$, except for $W(h)$ for which the full nonlinear wetting potential form (3) is used. For the

surface-energy term $\gamma\kappa$, noting that the surface curvature $\kappa = -\nabla \cdot [\nabla h/\sqrt{1+|\nabla h|^2}]$, we have $\gamma\kappa \sim -\gamma\nabla^2 h + \mathcal{O}(\hat{h}^3)$ and hence only need to keep the linear-order term in the second-order approximation considered here. To further simplify the calculation, we choose a length scale $l = \gamma/\mathcal{E}_0$ and a time scale $\tau = l^4/\gamma\Gamma_h$, where $\mathcal{E}_0 = 2E\epsilon_0^2(1+\nu)/(1-\nu)$ is the characteristic strain energy density, with ϵ_0 a reference misfit value. The resulting nondimensional dynamic equation for the perturbed surface profile $\hat{h}(\mathbf{q},t)$ is given by

$$\frac{\partial\hat{h}}{\partial t} = (-q^4 + \epsilon^{*2}q^3)\hat{h} - q^2\mathcal{W}_{\mathbf{q}}$$

$$- \epsilon^{*2}\sum_{\mathbf{q}'}\hat{h}(\mathbf{q}')\hat{h}(\mathbf{q}-\mathbf{q}')\Lambda(\mathbf{q},\mathbf{q}'),$$ (22)

where $\mathcal{W}_{\mathbf{q}}$ is the Fourier transform of the rescaled wetting potential $W(h)/\mathcal{E}_0$, $\epsilon^* = \epsilon_m/\epsilon_0$, and

$$\Lambda(\mathbf{q},\mathbf{q}') = q^2\left[(1-\nu)\frac{[\mathbf{q}'\cdot(\mathbf{q}-\mathbf{q}')]^2}{q'|\mathbf{q}-\mathbf{q}'|} - \mathbf{q}'\cdot(\mathbf{q}-\mathbf{q}')\right.$$

$$\left. + \nu q'|\mathbf{q}-\mathbf{q}'|\right] + \frac{2q}{q'}\left\{q_x(q_x - q_x')(q_x'^2 + \nu q_y'^2)\right.$$

$$+ q_y(q_y - q_y')(q_y'^2 + \nu q_x'^2) + (1-\nu)q_x'q_y'$$

$$\left. \times [q_x(q_y - q_y') + q_y(q_x - q_x')]\right\}.$$ (23)

In Eq. (22), the first term of the right-hand side is the combination of the surface-energy contribution and the

first-order elastic energy density $\hat{\mathcal{E}}^{(1)f}$, consistent with the previous linear-order results [6,31,34]. The last term is from the second-order perturbation result of the elastic energy density, i.e., Eq. (21) for $\hat{\mathcal{E}}^{(2)f}$. It would be straightforward, although with more complicated processes, to extend the above approach to incorporate higher-order contributions, based on the perturbation analysis of system elasticity given in Eqs. (9)–(14). That is, to obtain the nth-order elastic results, we can first express the nth-order expansion of the boundary conditions in terms of ξth-order ($\xi = 1,2,\ldots,n-1,n$) stress tensors [similar to the expression in Eq. (16)], and use it to calculate the nth-order solution of the displacement field given in Eq. (13). The corresponding film elastic properties can then be derived, particularly the nth-order elastic energy density $\hat{\mathcal{E}}^{(n)f}$ at the film surface which can be expressed as a function of ξth-order ($\xi = 1,2,\ldots,n-1$) elastic quantities that are already known. The corresponding higher-order evolution equation for $\hat{h}$ can be obtained by adding high-order terms $-q^2\hat{\mathcal{E}}^{(n)f}$ ($n > 2$) to Eq. (22).

This perturbation analysis given above is different from previous approximation methods which usually assumed small film surface slopes or gradients and/or different length scales along the lateral versus vertical direction of the film [31,33–35]. In our method, no such scale difference between lateral and vertical film directions is assumed and the small variable here is the Fourier component $\hat{h}(\mathbf{q})$ of surface height variation; thus, for our perturbation results of elastic energy and nonlinear film evolution equation (22) to be valid, surface height variations should be kept small, but not necessarily the surface slopes and gradients, and no condition on the lateral and vertical variation scales is imposed. The resulting higher-order elastic energy terms can be used to identify new mechanisms of strained island evolution, as will be detailed below.

Note that the above results can be applied to the study of both growing and nongrowing films. For a growing film with nonzero deposition rate v, the average film thickness $\bar{h}$ ($=h_0 + vt$) would grow with time, while the dependence of elastic energy density on film perturbation $\hat{h}$ would remain the same for both growing and nongrowing cases, so that the invariance of elastic energy density terms under transformation $h \rightarrow h + \text{const}$ is preserved (as in previous work of Refs. [6] and [35]). The explicit effect of $\bar{h}$ and nonzero v on film evolution is incorporated via the wetting term $\mathcal{W}_{\mathbf{q}}$ in Eq. (22). For simplicity, in the following we only focus on the case of nongrowing films with deposition rate $v = 0$ and examine the corresponding film evolution process.

IV. LINEAR STABILITY ANALYSIS

We first perform a linear stability analysis on Eq. (22) to determine the conditions of morphological instability of the system; such conditions are needed for the nonlinear calculations given in Secs. V and VI. Following the standard procedure, we assume an exponential growth $\hat{h} = \hat{h}_0 \exp(\sigma_h t)$ at early time, and apply it to the linearized evolution equation of $\hat{h}$. The characteristic equation for the perturbation growth rate σ_h is then given by

$$\sigma_h = -q^4 + q^3\epsilon^{*2} - q^2 a, \tag{24}$$

where $a = (w^*/h_{ml}^*)(x + \alpha_w)x^{-\alpha_w-1}e^{-x}$ as obtained from the linearization of the wetting potential $W(h)$, $x = \bar{h}/h_{ml}$, $w^* = w/\mathcal{E}_0$, and $h_{ml}^* = h_{ml}/l$. From the above dispersion relation, we can identify the condition for the occurrence of film morphological instability, which is given by $\epsilon^{*4} \geqslant 4a$ or, equivalently,

$$\frac{e^x x^{\alpha_w+1}}{x + \alpha_w} \geqslant \frac{4w^*}{\epsilon^{*4}h_{ml}^*}. \tag{25}$$

The corresponding characteristic wave number of film instability (for the fastest instability growth mode) can be written as

$$q_{\max} = \frac{3}{8}\left[\epsilon^{*2} + \sqrt{\epsilon^{*4} - \frac{32}{9}a}\right]. \tag{26}$$

Equation (25) is used to identify the parameters in our numerical simulations shown below, for which the initial film instability and hence the appearance of nonplanar surface morphology or islands are examined. Note that for given film conditions such as misfit strain ϵ_m and wetting parameters, Eq. (25) indicates that due to the film-substrate wetting effect (with $\alpha_w > 0$), the morphological instability and surface nanostructures will develop only for thick enough films, with the critical thickness $\bar{h}_c$ determined by Eq. (25), i.e., $e^{x_c}x_c^{\alpha_w+1}/(x_c + \alpha_w) = 4w^*/\epsilon^{*4}h_{ml}^*$ (where $x_c = \bar{h}_c/h_{ml}$); the value of $\bar{h}_c$ increases with smaller film-substrate misfit strain. Also, the characteristic size (or wavelength $\lambda = 2\pi/q_{\max}$) of surface structures at the initial stage will decrease with the increasing average film thickness $\bar{h}$, as can be obtained from Eq. (26).

V. EFFECTS OF WETTING POTENTIAL

To validate our model system and the nonlinear dynamic equation (22) derived above, we first examine the effect of wetting potential on film evolution and compare it to the well-known results of cusp formation obtained from previous full elasticity calculations [23,25]. Since Eq. (22) is already presented in Fourier space, in our numerical simulations we directly use the spectral method with periodic boundary conditions along the lateral x and y directions, and also an exponential propagation algorithm for time integration [46]. This allows us to use large enough time steps (up to $\Delta t = 1$ in most results shown below, except for the study of groove or cusp formation for which $\Delta t = 0.01$ is used). For rescaling parameters that are associated with the nondimensional equation (22), a reference misfit $\epsilon_0 = 3\%$ is chosen, and thus the length scale can be estimated as $l \simeq 5.5$ nm if using the material parameters of Ge/Si system.

As found first by Yang and Srolovitz [23] and later in various numerical studies of two-dimensional (2D) [25,28] and 3D [30,33] systems via solving either the full elasticity problem or the reduced nonlinear evolution equations, deep grooves or cusps will form in stressed solid systems without the incorporation of wetting effect. This is well reproduced in our numerical results of Eq. (22), as shown in Fig. 1 for 3% misfit films with $v = \frac{1}{3}$ and initial film thickness $h_0 = 0$. Two types of initial conditions are used: (1) a small random disturbance of a planar film of thickness h_0, with results of a 128×128 system presented in Figs. 1(a) and 1(b), and
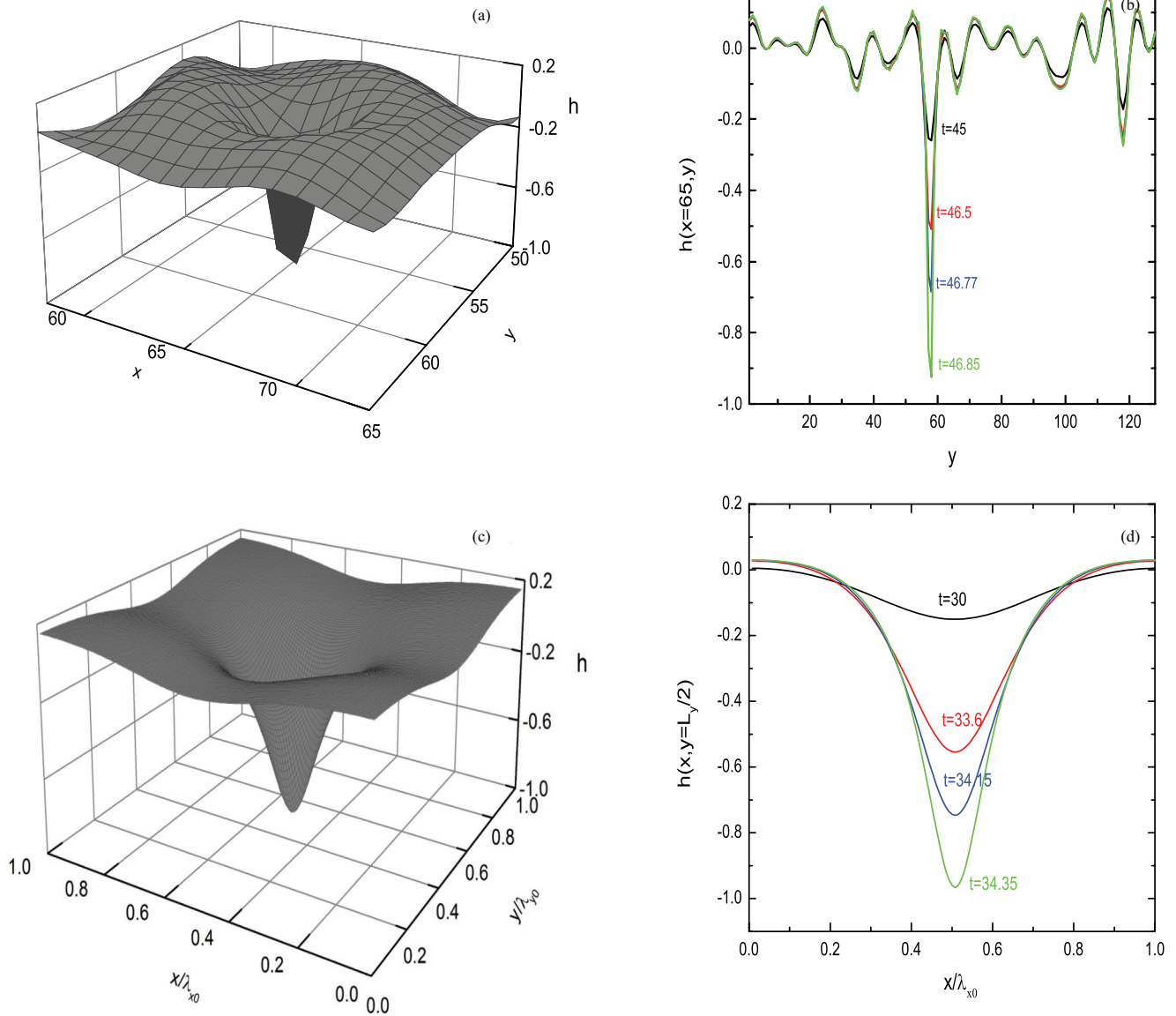
FIG. 1. (Color online) Surface morphologies of 3% strained films, as obtained from numerical simulations without the wetting effect. The simulations start either from small random initial perturbation of a planar film [(a) and (b)] or from a doubly periodic surface profile with wave vector $q_{x0} = q_{y0} = 3/4\sqrt{2}$ and amplitude $A_0 = 0.01$ [(c) and (d)]. Both 3D morphologies, (a) at $t = 46.77$ for a portion of a 128×128 system and (c) at $t = 34.35$ for system size $\lambda_{x0} \times \lambda_{y0}$, and also time evolution of 2D cross-section profiles are shown.

(2) a weakly perturbed film with doubly periodic sinusoidal surface profile $h = h_0 + A_0[\cos(q_{x0}x) + \cos(q_{y0}y)]$, as given in Figs. 1(c) and 1(d) for a $\lambda_{x0} \times \lambda_{y0}$ system (where $\lambda_{x0} = 2\pi/q_{x0}$ and $\lambda_{y0} = 2\pi/q_{y0}$). For condition (2), the initial perturbed amplitude is set as $A_0 = 0.01$, and a perturbed wave vector $q_{x0} = q_{y0} = 3/4\sqrt{2}$ is chosen, corresponding to the wave number of the most linearly unstable mode determined by Eq. (26). In both cases, the formation of singular cusps or deep grooves and their rapid growth have been found during the film evolution, as evidenced by the 3D morphological profiles given in Figs. 1(a) and 1(c), and also from the results of time-evolving 2D cross-section profiles shown in Figs. 1(b) and 1(d), which are consistent with the previous 2D results of Spencer and Meiron [25] and Xiang and E [28].

To incorporate the wetting effect, in our calculations we use a pseudospectral method; that is, we first evaluate the wetting potential $W(h)$ from Eq. (3) in real space and then obtain its Fourier component $\mathcal{W}_{\mathbf{q}}$ as used in the dynamic equation (22). As expected, the cusp or groove singularity is completely suppressed by the film-substrate wetting interaction since the wetting potential tends to preserve a finite-thickness wetting layer on the substrate and prevent its depletion [see Eq. (3) for the singularity and infinite energy penalty of $W(h)$ when $h \to 0$]; arrays of strained islands or quantum dots will then form and grow. This has been verified by our numerical results shown in Fig. 2, where we have used the parameters of $\epsilon_m = 3\%$, $h_0 = 0.41$, $h_{ml}^* = 0.3$, $\alpha_w = 2$, $w^* = 0.08$ or 0.2, and simulation time step $\Delta t = 1$. However, another type of
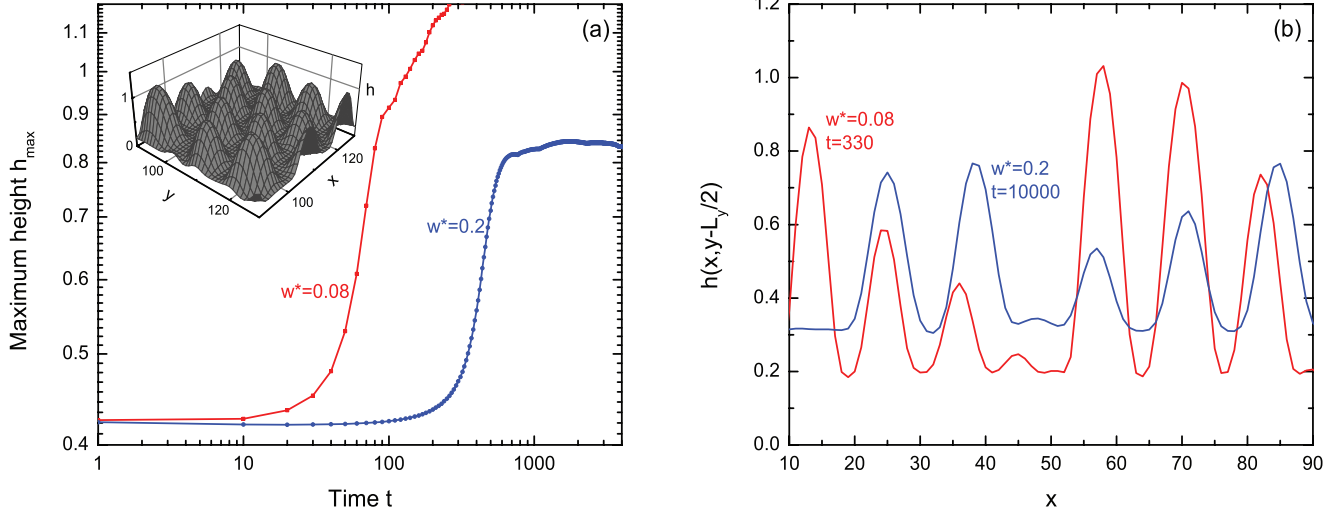
FIG. 2. (Color online) Time evolution of 3% strained films with different wetting strength $w^* = 0.08$ and 0.2. (a) Evolution of maximum surface height, with a 3D island morphology for $w^* = 0.08$ at $t = 330$ shown in the inset; (b) 2D cross-section profiles at $y = L_y/2$ for $w^* = 0.08$ at $t = 330$ and $w^* = 0.2$ at $t = 10\,000$.

growth instability would occur when the strength of wetting interaction is not strong enough (e.g., $w^* = 0.08$ in Fig. 2), showing as the rapid increase of island heights beyond initial time stage and then the blowup of numerical solution at late times. Such instability with unbound growth of island height is absent for stronger wetting effect, such as the effect of $w^* = 0.2$ shown in Fig. 2(a), which gives the stabilization of island evolution. This can be understood from the fact that the wetting interaction tends to prevent the depletion of the film-substrate wetting layer and hence suppresses the mass transport from the valley of an island to its top, leading to the constraint of island height as a result of mass conservation. Such effect would increase with the strength of wetting interaction, as can be seen from the results given in Fig. 2(b): thicker film layers between surface islands and shallower valleys are found for larger wetting strength w^*, as a result of stronger suppression on the valley-to-peak diffusion process.

VI. RESULTS OF NONLINEAR EVOLUTION

To examine the detailed evolution of strained film morphology more systematically, we have conducted numerical simulations of the nonlinear dynamic equation (22) for different small film-substrate misfit strains $\epsilon_m = 2\%$, 2.5%, and 3% (in such weak strain limit, the continuum elasticity approach can be well applied, as shown in most recent studies [42]). The parameters for the wetting potential are chosen as $h_{ml}^* = 0.3$, $\alpha_w = 2$, and $w^* = 0.2$, with all other parameters the same as those given in Sec. V. In our simulations, we have used three different system sizes $L_x \times L_y$ for each parameter set, including the lateral dimensions of 128×128, 256×256, and 512×512, to examine any possible artifacts of finite size effects. A numerical grid spacing $\Delta x = \Delta y = 1$ is adopted, and the integration time step is chosen as $\Delta t = 1$. The quantitative results given below have been averaged over 20 independent runs for system sizes 128×128 and 256×256, and 10 runs for 512×512. Also, each simulation starts

with a rescaled initial film thickness of $h_0 = 0.67$ for misfit strain $\epsilon_m = 2\%$, $h_0 = 0.5$ for $\epsilon_m = 2.5\%$, and $h_0 = 0.41$ for $\epsilon_m = 3\%$, all of which are within the corresponding instability parameter region for each misfit as determined by Eq. (25).

Typical simulation results of film evolution and the formation and dynamics of quantum dot arrays are illustrated in Fig. 3, for 2.5% mismatch between the film and substrate. At the beginning stage, surface undulations occur due to the film morphological instability determined in Eq. (25), leading to the formation of strained surface islands or quantum dots as shown in Fig. 3(a). Note that at different surface locations, islands will form and grow gradually at different rates due to the nonlinear effects of elastic interaction. Island coarsening occurs at the next stage, showing as the growth of some quantum dots at the expense of other shrinking ones and hence the decrease of island density on the film surface. This can be seen more clearly in the corresponding 2D top-view images of Figs. 3(d)–3(f), which give the comparison of island distribution between times $t = 1000$, 2000, and 10^4. Such coarsening process becomes much slower as time increases, and the system would approach an asymptotic state with steady arrays of strained quantum dots. As expected, this late-time state of film surface structures highly depends on the value of film-substrate misfit strain, with an increase of island density and a decrease of island spacing for larger misfits. This has been confirmed in our results of 2% and 3% films given in Fig. 4, as compared to the 2.5% film shown in Figs. 3(c) and 3(f). In our simulations, no long-range spatial order can be found for quantum dot arrays, even at the late-time stage, agreeing with the observation of most experimental and theoretical studies.

To quantify the above results, we have analyzed the film surface morphology through various time-dependent parameters, including the structure factor of surface height, its moments, the maximum height of surface profile, and the surface roughness, as shown in Figs. 5–8 with results of different system sizes presented. The structure factor is defined as $S(q,t) = \langle |\hat{h}(\mathbf{q},t)|^2 \rangle_{\hat{q}}$, with a circular average over orientation $\hat{q}$ of the wave vector. Typical results of $S(q,t)$ are
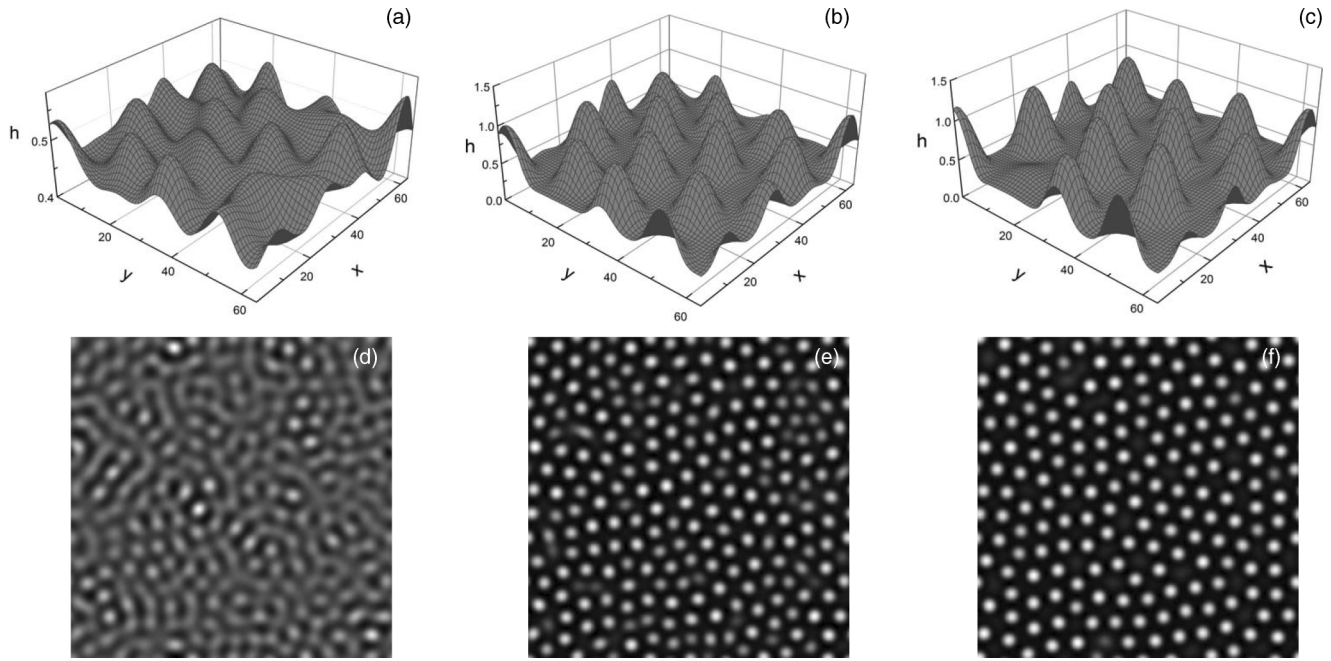
FIG. 3. Morphological profiles of a 2.5% strained film, at simulation times $t = 1000$ [(a) and (d)], 2000 [(b) and (e)], and 10 000 [(c) and (f)]. A fraction of 3D morphologies in a 256 × 256 system is given in panels (a)–(c), while the corresponding 2D grayscale top-view images of the full system size are shown in (d)–(f).

given in Fig. 5 for different misfit strains of 2%, 2.5%, and 3%. As the misfit increases, the wave number related to the peak location of the structure factor becomes larger, corresponding to smaller island spacing and also higher quantum dot density
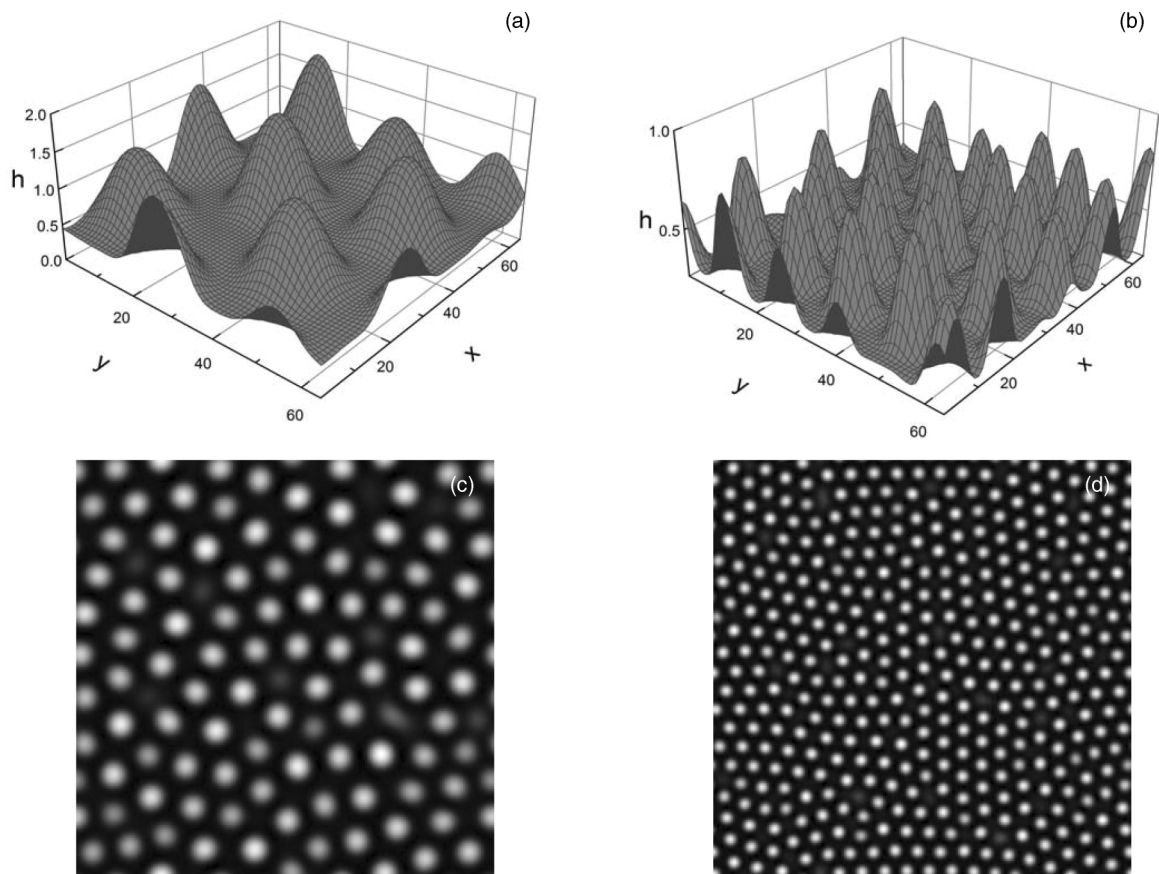

FIG. 4. Morphological profiles of (a) 2% and (b) 3% strained films at late time stage of $t = 10\,000$. Only a portion of the 256 × 256 system is shown in the 3D images of (a) and (b). The corresponding 2D top-view images of the full system size are given in (c) and (d).
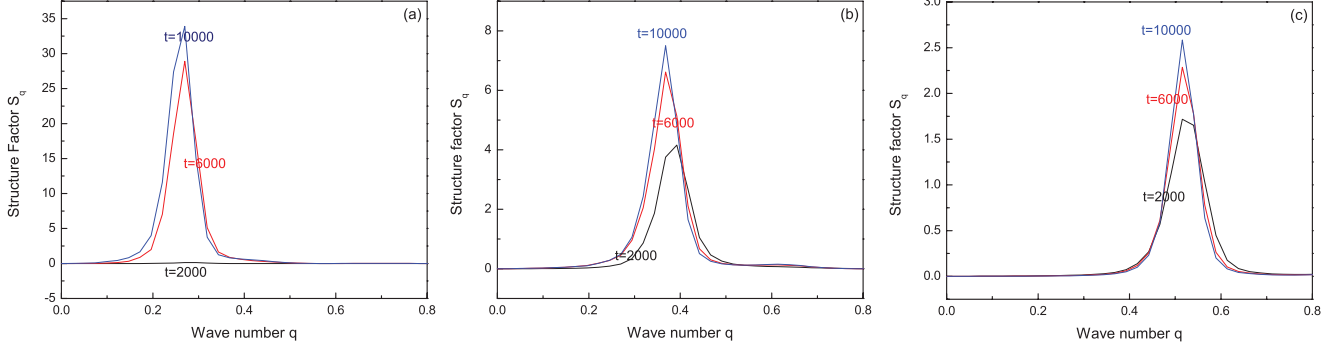
FIG. 5. (Color online) Structure factor of the surface height as a function of wave number q, for different misfits (a) $\epsilon_m = 2\%$, (b) $\epsilon_m = 2.5\%$, and (c) $\epsilon_m = 3\%$, system size 256×256, and times $t = 2000$, 6000, and 10000.

as already seen in Figs. 4(c), 3(f), and 4(d). Also, for smaller misfit strain, larger time is needed for the initial formation of islands [if we compare the $t = 2000$ curves in Figs. 5(a)–5(c)], consistent with the result of σ_h in the linear stability analysis.

Details of the time evolution of quantum dot islands can be characterized by the calculation of various moments of the structure factor. The nth moment of $S(q,t)$ is defined as

$$m_n(t) = \frac{\int dq \, q^n S(q,t)}{\int dq \, S(q,t)}, \qquad (27)$$

which yields the information of the characteristic size and spatial scale of surface structures [47]. We have calculated the first three moments of $S(q,t)$, with time evolution results for three different misfits given in Figs. 6(a) (for m_1), 6(b) (for m_2), and 6(c) (for m_3). Three characteristic regimes of film evolution can be identified in each simulation: the process of surface instability development and island formation at early times, coarsening of these strained islands at intermediate stage, and an asymptotic stage of island array stabilization at late times. The first two stages can be distinguished clearly in the results of moments shown in Fig. 6, as separated by the

turning point (i.e., maximum of m_n) of the time evolution curve for each moment. The increase of m_n at the first time stage is due to the continuous appearance of new islands at various times as observed in our simulations, and thus the decrease of average island spacing. The time range of this early stage of island formation is longer for smaller misfit strain, as a result of overall smaller instability growth rate [see Eqs. (24)–(26)]. This has been verified in Fig. 6, via comparing the three panels of misfits 3%, 2.5%, and 2% (from top to bottom) for results of each moment.

Once most islands have formed (i.e., when the moments m_n reach maximum values), they start to coarsen so that the average distance between islands increases, leading to the decrease of m_n. A power-law behavior of coarsening, $m_n(t) \sim t^{-\beta_n}$, can be obtained, but such behavior is limited to a transient time range at the beginning of the coarsening stage. As shown in Fig. 6, this time range is smaller for larger film-substrate misfit strain ϵ_m, with faster crossover to a saturated state. Also, slower coarsening rate has been found for larger misfit, corresponding to smaller coarsening exponents β_n, which are identified as follows
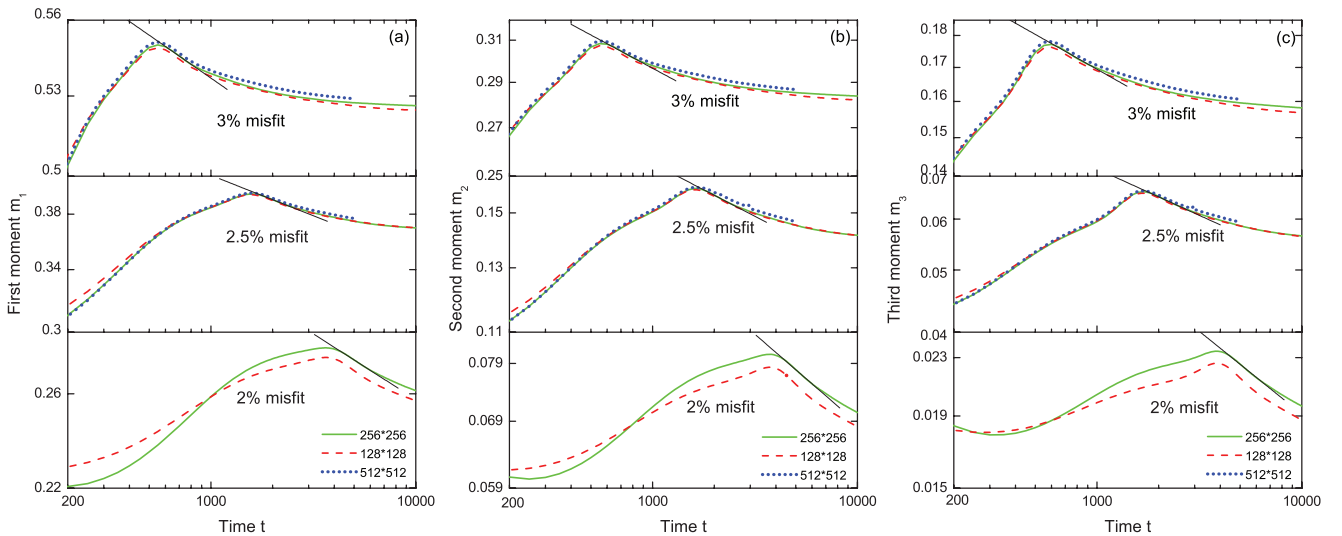

FIG. 6. (Color online) Time evolution of the three moments of structure factor: (a) m_1, (b) m_2, and (c) m_3, for misfit strains $\epsilon_m = 2\%$, 2.5%, and 3%. The solid lines represent the simulation results of grid size 256×256, whereas the dashed and dotted lines represent the results for grid sizes 128×128 and 512×512, respectively. Power-law fittings (i.e., the thin lines) at the beginning of coarsening stage for the 256×256 system are also shown.
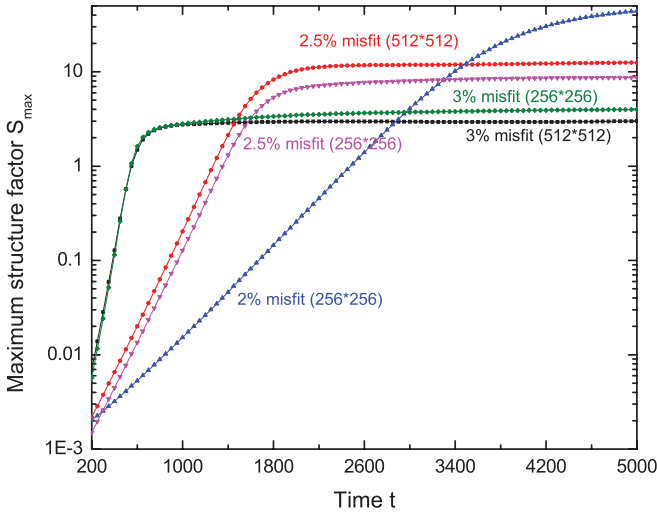
FIG. 7. (Color online) Time evolution of the maximum value of structure factor, for misfits $\epsilon_m = 2\%, 2.5\%$, and 3%. Results for different system sizes 256×256 and 512×512 are shown for comparison.

(for system size 256×256): for $\epsilon_m = 2\%$, $\beta_1 = 0.1010 \pm 0.0008$, $\beta_2 = 0.181 \pm 0.002$, and $\beta_3 = 0.235 \pm 0.003$; for $\epsilon_m = 2.5\%$, $\beta_1 = 0.0702 \pm 0.0007$, $\beta_2 = 0.120 \pm 0.002$, and $\beta_3 = 0.145 \pm 0.004$; for $\epsilon_m = 3\%$, $\beta_1 = 0.0449 \pm 0.0009$, $\beta_2 = 0.076 \pm 0.003$, and $\beta_3 = 0.090 \pm 0.006$. Note that if the structure factor is assumed to obey a simple dynamic scaling behavior due to coarsening, one would usually expect that $m_n(t) \sim t^{-n\beta_1}$; i.e., $\beta_n = n\beta_1$. However, the above results of coarsening exponents in the intermediate time range for all different misfit strains do not support this assumption, and we cannot identify a simple format of scaling for the structure factor. This might be attributed to the complex relaxation of strain energy in the film and the nonlinear elastic interaction between surface islands [see, e.g., Eq. (23)] which are more complicated than that revealed by simple scaling.

These two regimes of island formation and coarsening are also illustrated in our numerical results for the maximum
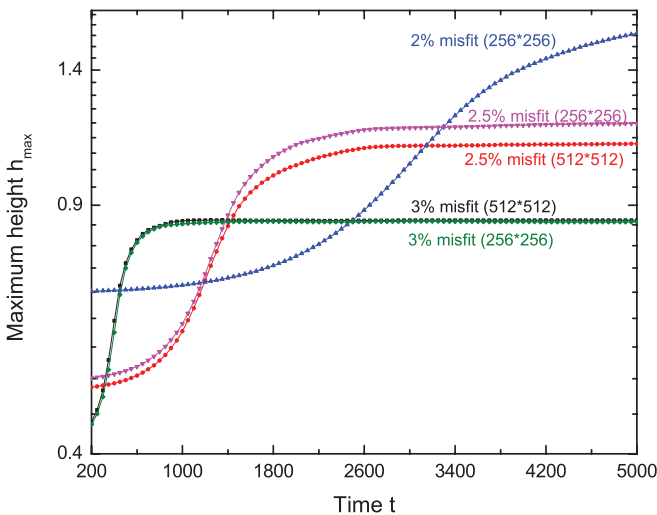

FIG. 8. (Color online) Time evolution of maximum surface height for misfits $\epsilon_m = 2\%, 2.5\%$, and 3% and system sizes 256×256 and 512×512.
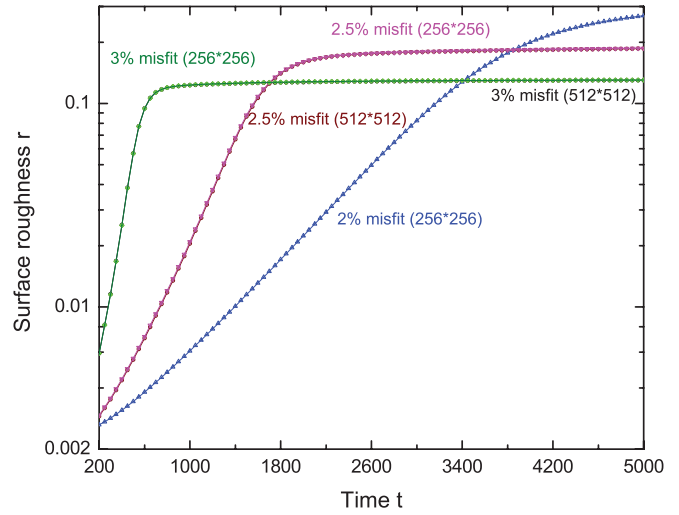

FIG. 9. (Color online) Time evolution of surface roughness for various misfits $\epsilon_m = 2\%, 2.5\%$ and 3%. Note that for each misfit, results of different system sizes 256×256 and 512×512 almost overlap with each other.

value of the structure factor S_{max} (Fig. 7), the maximum surface height h_{max} (Fig. 8), and the surface roughness $r(t) = \langle (h - \bar{h})^2 \rangle^{1/2}$ (Fig. 9). The growth of all three quantities can be observed during the first stage of instability growth and island formation, which corresponds to the same initial time range as the m_n results shown in Fig. 6. Both S_{max} and the roughness $r(t)$ grow exponentially with time at this stage, consistent with the behavior of linear instability analyzed in Sec. III. However, at later times during the coarsening process, these quantities show rather slow growth and an approach to saturation, even for h_{max}. Such phenomenon of saturating surface roughness has been obtained in a recent study of a nonlinear evolution equation [33], but not in other studies using different evolution equations (which instead observed power-law growth) [34,35]. The limited growth of maximum surface height given in Fig. 8 during island coarsening has not been reported in these previous works, which usually showed a faster growth of h_{max} such as a power-law behavior [34]. Such discrepancy can be attributed to different approximations used in these studies: A long-wave approximation was used in Refs. [34,35], assuming large lateral variation along the film surface as compared to the vertical direction, while in Ref. [33] an expansion on small surface height gradient was conducted without such assumption of length scale difference. Also, only first-order elastic energy was considered in Ref. [34], while in both Refs. [33] and [35] up to second-order elastic terms have been included. As described in Sec. III, our approach here is different from these previous analyses, with no assumption and constraint on either the length scale contrast between different directions or the magnitude of surface slopes or gradients. This allows us to better identify the important role played by the high-order elastic energy terms, as will be detailed in Sec. VII.

Our simulation results also indicate a crossover from the island coarsening regime to an asymptotic state of steady quantum dot arrays, showing as saturated values of S_{max}, h_{max}, and $r(t)$ (see the 2.5% and 3% results in Figs. 7–9), and more clearly, the saturation of m_n given in Fig. 6. Such crossover

can be identified through the slowing of the m_n decay after the transient of power-law-type coarsening, and occurs earlier for larger misfit strain. To exclude any artifacts from finite size effects, we have tested our simulations for different system sizes ranging from 128×128 to 512×512, with qualitatively similar results obtained. This phenomenon of slowing and saturation of coarsening process and the resulting stabilization of island arrays has been found in some experiments of post-growth Ge/Si systems [17,19] and also in some modeling and simulation results based on either direct solution of system elasticity [26,32] or reduced film evolution equations [33,45]; however, no sign of coarsening termination in post-deposition films has been shown in some other experimental [20] and theoretical [29,34,35] work. Note that in most theoretical studies showing the phenomenon of island stabilization, the effect of surface-energy anisotropy has been incorporated, which is different from the model used here (see the further discussion given below). Also, the effect of different misfit strains on island coarsening and stabilization, which is shown important from our above results, has not been addressed in most previous studies. Our results given above suggest that much longer times are needed to observe the slowing or cessation of island coarsening for smaller misfits, which could be useful for addressing the discrepancy of experimental observation: For example, the stabilization of quantum dot growth can be found at relatively short growth-temperature annealing times for Ge/Si(001) system with large misfit ($\sim$4%) [17,19], while it is more difficult to observe in SiGe/Si(001) experiments with weak misfit strain ($<$1%) [20].

VII. DISCUSSION

To understand the mechanisms underlying the phenomenon of island stabilization given above, it would be helpful to examine the effects of all contributed terms in the evolution equation (22). As already discussed in Sec. V, the wetting potential plays a crucial role on the stabilization of surface morphology via limiting the valley-to-peak mass transport and thus the growth of island height. Similar mechanism is expected during island coarsening, and the stabilization effect of wetting potential should be also important for the island size saturation. On the other hand, the dynamics of coarsening involves the redistribution of mass between different islands, a process that can not be constrained by the wetting effect as long as the wetting layer is not depleted. Thus, additional factor(s) must be in play to account for the island stabilization process.

To further illustrate the stabilization process, we show in Fig. 10 the time-varying profiles of the chemical potential $\mu = \gamma\kappa + W + \mathcal{E}^f$ at the film surface and also its corresponding elastic contribution $\mathcal{E}^f$ (i.e., the surface elastic energy density). For simplicity, only the cross-section results at $x = L_x/2$ are presented, for an example of 2.5% misfit film. Smaller spatial variations of chemical potential μ along the film surface are obtained at later times [note the very small vertical scale in Fig. 10(a)], indicating an approach to an asymptotic saturated state. This is consistent with the results given in Figs. 6–9 for various morphological properties, and also with the evolution profiles of elastic energy density $\mathcal{E}^f$ given in Fig. 10(b). Furthermore, in Fig. 11 we examine the detailed mechanisms
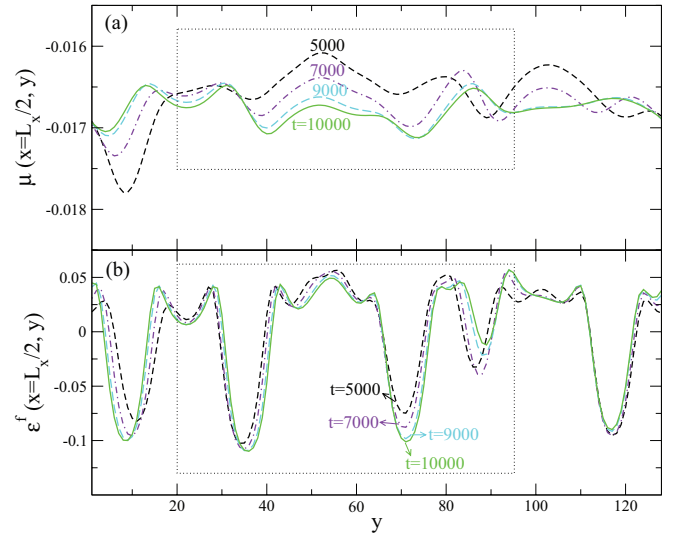

FIG. 10. (Color online) Cross-section profiles of (a) surface chemical potential μ and (b) elastic energy density $\mathcal{E}^f$, for misfit $\epsilon_m = 2.5\%$ and different times $t = 5000, 7000, 9000,$ and 10 000. The boxed region will be further studied in Fig. 11.

of such saturation through identifying the time evolution of various components of chemical potential, including the surface-energy contribution $\gamma\kappa$ and the first- and second-order elastic energy densities $\mathcal{E}^{(1)f}$ and $\mathcal{E}^{(2)f}$. We focus on a small region of four islands [see Fig. 11(a)], representing three scenarios of quantum dot evolution: (1) large islands that are growing and stabilizing, (2) small islands that are shrinking
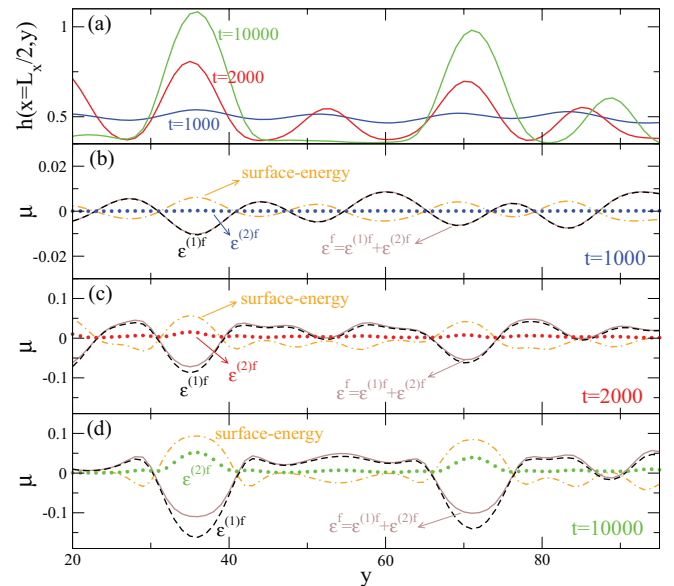

FIG. 11. (Color online) Cross-section profiles of (a) surface morphology and (b)–(d) various energy densities, for 2.5% misfit and times $t = 1000$ (at early stage of instability and island formation), 2000 (island coarsening stage), and 10 000 (stabilization stage). Different components of the film surface chemical potential are shown, including the surface-energy contribution (dotted-dashed orange curves), first-order elastic energy density $\mathcal{E}^{(1)f}$ (dashed black), second-order elastic density $\mathcal{E}^{(2)f}$ (green stars), and the total elastic contribution $\mathcal{E}^f = \mathcal{E}^{(1)f} + \mathcal{E}^{(2)f}$ (solid brown).

[see the middle island in Fig. 11(a)], and (3) islands that are migrating (see the one at the right corner). As expected from previous analysis [6], for an undulated surface (i.e., in the region of surface islands), the strain energy is concentrated at surface valleys but released at peaks; the resulting surface elastic energy density gradient would drive the diffusion process from the valleys to peaks and thus the growth of surface islands. On the other hand, this morphological destabilization process is competed by the stabilization effect of surface energy, showing as energy penalty for high-curvature surface areas and hence a spatial distribution opposite to that of elastic density (see the dotted-dashed curves). This classical view of quantum dot formation has been well reproduced in our results of all three evolution stages: the early morphological instability shown in Fig. 11(b) (at $t = 1000$), a coarsening regime in Fig. 11(c) (at $t = 2000$), and an island stabilization stage in Fig. 11(d) (at $t = 10\,000$).

For islands to be stabilized, one would expect mechanisms of film evolution involving additional energy penalty for large, increasing island size, so that the overall stabilization factors would compensate and suppress the destabilization effect (i.e., continuing growth and coarsening of surface islands) caused by stress relaxation. In previous studies, such factors are usually provided by additional surface-energy terms, particularly the surface-energy anisotropy, which has been shown to enhance the surface-energy stabilization effect, constrain the island height, and lead to island shape or facet selection and transition [16,17]; this effect of surface anisotropy has been deemed essential for the existence of steady island arrays in some previous theoretical work (with various assumptions of the wetting effect) [26,32,45]. However, in this work we only consider isotropic surface energy. In addition to the wetting effect (which is also related to the surface energy as a result of the h dependence of γ_s), what we identify here is a factor that is due to the contribution of higher-order perturbed elastic energy on the interaction and evolution of surface islands, as detailed in Fig. 11: Positive contribution from the second-order elastic energy density $\mathcal{E}^{(2)f}$ is found for large surface islands, showing as an effective energy-penalty term and hence a reduction of strain relaxation effect. [Note that this result is still compatible with the well-known strain relaxation mechanism since the total elastic density $\mathcal{E}^f$ still shows a destabilization effect due to the dominance of first-order density $\mathcal{E}^{(1)f}$; see Figs. 11(c) and 11(d).] Such effect of $\mathcal{E}^{(2)f}$ becomes important only at late stage with large enough islands, and is negligible for small ones, as seen from the comparison between Figs. 11(b)–11(d).

To understand this seemingly counterintuitive result, which is beyond the conventional view based on linear instability analysis, we examine the detailed expression of $\mathcal{E}^{(2)f}$ which, from Eqs. (21)–(23), is rewritten as

$$\mathcal{E}^{(2)f}(\mathbf{r}) = \epsilon^{*2}\left[f(h) + \int d\mathbf{r}' \int d\mathbf{r}'' h(\mathbf{r}') \right.$$
$$\left. \times\, G(\mathbf{r}-\mathbf{r}',\mathbf{r}'-\mathbf{r}'')h(\mathbf{r}'') \right], \qquad (28)$$

where

$$f(h) = |\nabla h|^2 + \nu(\mathcal{E}^{(1)f}/\epsilon^{*2})^2 + (1-\nu)\sum_{i=1}^{3} g_i^2(h), \quad (29)$$

with $g_i(h)$ ($i = 1,2,3$) the Fourier transform of $q_x^2\hat{h}/q$, $q_y^2\hat{h}/q$, and $\sqrt{2}q_xq_y\hat{h}/q$, respectively, and

$$G(\mathbf{r}-\mathbf{r}',\mathbf{r}'-\mathbf{r}'')$$
$$= \sum_{\mathbf{q},\mathbf{q}'} e^{i\mathbf{q}\cdot(\mathbf{r}-\mathbf{r}')+i\mathbf{q}'\cdot(\mathbf{r}'-\mathbf{r}'')}\frac{2}{qq'}\left\{ q_x(q_x - q_x')(q_x'^2 + \nu q_y'^2) \right.$$
$$+ q_y(q_y - q_y')(q_y'^2 + \nu q_x'^2) + (1-\nu)q_x'q_y'$$
$$\left. \times\, [q_x(q_y - q_y') + q_y(q_x - q_x')] \right\}. \qquad (30)$$

In Eq. (28), the first part $f(h)$ is always positive, analogous to the "self"-elastic-energy of a given surface profile that serves as an energy penalty to suppress its coarsening; the second part represents the correlation between surface heights and thus the elastic interaction between surface islands. Within each island region (particularly near the peak), the magnitudes of both parts increase with the island size as verified in our numerical calculations.

If these second-order elastic contributions are absent or not strong enough, the elastic energy relaxation would increasingly dominate over the surface-energy stabilization effect, driving the continuing island growth even in the presence of the wetting potential. This can be illustrated clearly from our numerical results given in Fig. 12, where the same film evolution equation (22) is simulated, but with only first-order elastic energy $\mathcal{E}^{(1)f}$ incorporated. All other parameters remain unchanged, including the same wetting potential approximation Eq. (3). The maximum surface height is found to increase monotonically with time [see Fig. 12(a)], without any slowing or stabilization process observed, a result that is consistent with previous work [34]. Time evolution of the corresponding 2D cross-section surface profiles is given in Fig. 12(b), from which two main features of surface dynamics can be identified: (1) Large mass transport from film layers to islands is observed, leading to much thinner film layers between surface islands as compared to the result shown in Fig. 11(a), which incorporates the second-order elastic energy effects. Although the wetting potential still has the effect of preserving the wetting layer in-between surface islands and then limiting the diffusion process from the depleted wetting layer to the peaks, here such effect becomes relatively weaker as time evolves due to the increasing dominance of the destabilization effect of first-order elastic energy and the absence of the "self"-energy penalty term $f(h)$ for large islands. (2) Mass transport between islands continues to occur, which corresponds to island migration or coarsening process and is actually a secondary effect compared to (1); this process can not be prevented by the wetting effect, and can be controlled only by the higher-order elastic energy terms describing island interaction and correlation [see Eq. (28)]. Thus, at late times the island heights increase rapidly, resulting in the formation of surface islands with large aspect ratio between height and width as shown in Fig. 12. The perturbation method used here is no longer valid for such high islands, and the simulations will ultimately blow up. This is qualitatively different from the results given above with the incorporation of second-order elastic energy, where islands with well constrained aspect ratio are obtained, which also shows the applicability of the perturbation method developed here.
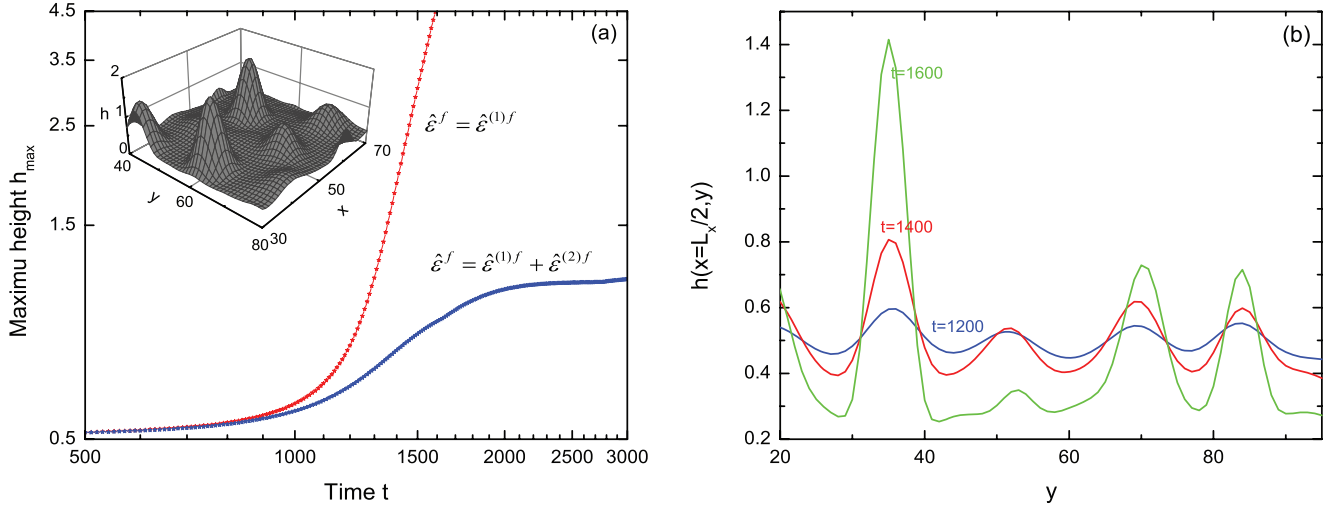
FIG. 12. (Color online) Results of strained film evolution with only first-order elastic energy $\mathcal{E}^{(1)f}$ incorporated. All other parameters are the same as those in Figs. 10 and 11. (a) Maximum surface height as a function of time t, with results from calculations up to second-order elastic energy (with $\mathcal{E}^f = \mathcal{E}^{(1)f} + \mathcal{E}^{(2)f}$) also shown for comparison; a sample 3D image of island morphology at $t = 1600$ is presented in the inset. (b) 2D cross-section profiles of film surface morphology at different times.

All these results indicate that the nonlinearities given by the higher-order strain energy of individual islands and the elastic interaction between islands can affect the pathway of film strain relaxation at late evolution times, slow down the decrease of total elastic energy via their increasing positive energy contribution for large islands, and thus effectively reduce the effect of stress relaxation as the surface instability driving force. Such reduction leads to a relatively stronger role played by the surface energy and the wetting potential at later times [see the comparison between Figs. 11(c) and 11(d), and between Figs. 11(a) and 12(b)], limiting the mass transport between film layers and islands and hence suppressing the island growth and coarsening. Note that these results and mechanisms identified here are based on our calculations up to second-order perturbation of surface morphology. Incorporating third- or higher-order perturbation terms, which are not studied here, may add either positive or negative contributions to the elastic energy density. However, such additional contributions would be much smaller due to their high-order nature, and thus even if their net contribution to the elastic energy becomes negative, it could only reduce, but not completely offset, the effect of positive $\mathcal{E}^{(2)f}$; this would lead to longer time stage of island coarsening and the postponing of the asymptotic saturated state, but the major results of island stabilization given above will still persist.

VIII. CONCLUSIONS

We have investigated the nonlinear dynamic processes governing the formation, coarsening, and stabilization of strained quantum dot islands on the surface of heteroepitaxial films, through the application of a nonlinear evolution equation for film morphology. Our study is based on a continuum elasticity model that incorporates the film-substrate wetting effect and, importantly, on the construction of a perturbation method in Fourier space for determining the system elastic properties. Different from previous analyses based on long-wave or

small-slope approximations, our approach does not impose assumptions about the variation length scales or surface slopes of the film, and allows us to well examine the important effect of high-order elastic energy, particularly on the island stabilization process. In addition to a linear stability analysis which yields the conditions of film morphological instability, we have performed large scale numerical calculations of the dynamic equation derived to study the detailed behavior of post-growth film evolution. We focus on effects of small misfit strains which correspond to relatively large length scale of surface nanostructures, and analyze the evolution of strained surface islands using a variety of characteristics of film morphology, including the structure factor of surface height, its first three moments, the maximum height of surface profile, and the surface roughness.

Consistent with previous experimental and theoretical work, our results have shown three characteristic stages of island evolution for post-deposition films, including (1) the early stage of morphological instability and island formation, as characterized by the exponential growth of maximum structure factor S_{max} and the surface roughness as well as the increase of maximum surface height and moments m_n; (2) a nonlinear island coarsening stage, with a transient power-law behavior of m_n decay that appears at the beginning of this stage; and (3) a crossover to an asymptotic state of stabilized island arrays (although without long-range spatial order), after the slowing and suppression of coarsening process. Also, the dependence of these detailed properties on the film-substrate misfit strain has been obtained, such as the values of coarsening exponents and the time ranges for the crossover between different evolution stages. These have been shown important for the understanding of different, or seemingly inconsistent, experimental results, particularly for the late-time stage of island coarsening or stabilization. On the other hand, such dependence does not qualitatively affect our results of the three evolution regimes; the same conclusion can be drawn for the effect of different finite system sizes used in our

simulations. To understand the mechanisms underlying the nonlinear evolution of strained films, we have examined the effects of film-substrate wetting potential, in particular its role on the suppression of the valley-to-peak mass diffusion process that would lead to wetting layer depletion, and its constraining effect on island growth. Furthermore, through a detailed study of the time evolution of elastic energy density distribution at the film surface, we find that higher-order terms of film elastic energy, which incorporate the interaction between strained surface islands and the higher-order "self"- elastic-energy of individual islands, can effectively alter the relaxation pathway of film strain energy at late stage. They play an important role on the saturation of coarsening process and

stabilization of quantum dot arrays, in particular the crossover to a saturated state with balanced multi-island interactions and limited island-layer and between-island mass transport. Thus, our results indicate that both effects of film-substrate wetting interaction and high-order elastic energy are pivotal for the achieving of steady quantum dot arrays and also for the understanding of the self-assembly process of strained film heteroepitaxy.

ACKNOWLEDGMENT

APPENDIX

Based on the perturbation analysis of system elasticity described in Sec. III, we have obtained the first- and second-order results of elastic stress tensors at the film surface. To first order of ε we have

$$\varepsilon\hat{\sigma}_{xx}^{(1)f}(\mathbf{q}) = \frac{2E\epsilon_m}{q(1-\nu)}\big(q_x^2 + \nu q_y^2\big)\hat{h}(\mathbf{q}), \quad \varepsilon\hat{\sigma}_{yy}^{(1)f}(\mathbf{q}) = \frac{2E\epsilon_m}{q(1-\nu)}\big(q_y^2 + \nu q_x^2\big)\hat{h}(\mathbf{q}), \quad \varepsilon\hat{\sigma}_{zz}^{(1)f}(\mathbf{q}) = 0,$$

$$\varepsilon\hat{\sigma}_{xy}^{(1)f}(\mathbf{q}) = 2E\epsilon_m\frac{q_xq_y}{q}\hat{h}(\mathbf{q}), \quad \varepsilon\hat{\sigma}_{xz}^{(1)f}(\mathbf{q}) = -\frac{E\epsilon_m}{1-\nu}iq_x\hat{h}(\mathbf{q}), \quad \varepsilon\hat{\sigma}_{yz}^{(1)f}(\mathbf{q}) = -\frac{E\epsilon_m}{1-\nu}iq_y\hat{h}(\mathbf{q}),$$
(A1)

while the results for second-order perturbation are given by

$$\varepsilon^2\hat{\sigma}_{xx}^{(2)f}(\mathbf{q}) = -\frac{E\epsilon_m}{1-\nu}\sum_{\mathbf{q}'}\left\{4\frac{q_x(q_x - q_x')}{q^3q'}\big(\nu q_y'^2 + q_x'^2\big)\big(q^2 + \nu q_y^2\big) + 4\nu\frac{(q_y - q_y')q_y^3}{q^3q'}\big(q_y'^2 + \nu q_x'^2\big)\right.$$

$$+ 4(1-\nu)\frac{q_x'q_y'}{q^3q'}[q_x(q_y - q_y') + q_y(q_x - q_x')]\big(q_x^2 + \nu q^2\big) - \frac{1}{q^2}[q_x'(q_x - q_x') + q_y'(q_y - q_y')]\big(2\nu q_y^2 + q_x^2\big)$$

$$+ 4(1-\nu)\frac{q_xq_yq_x'q_y'}{q^3q'}[q_y(q_y - q_y') - q_x(q_x - q_x')]\bigg\}\hat{h}(\mathbf{q}')\hat{h}(\mathbf{q} - \mathbf{q}'),$$
(A2)

$$\varepsilon^2\hat{\sigma}_{yy}^{(2)f}(\mathbf{q}) = -\frac{E\epsilon_m}{1-\nu}\sum_{\mathbf{q}'}\left\{4\frac{q_y(q_y - q_y')}{q^3q'}\big(\nu q_x'^2 + q_y'^2\big)\big(q^2 + \nu q_x^2\big) + 4\nu\frac{(q_x - q_x')q_x^3}{q^3q'}\big(q_x'^2 + \nu q_y'^2\big)\right.$$

$$+ 4(1-\nu)\frac{q_x'q_y'}{q^3q'}[q_x(q_y - q_y') + q_y(q_x - q_x')]\big(q_y^2 + \nu q^2\big) - \frac{1}{q^2}[q_x'(q_x - q_x') + q_y'(q_y - q_y')]\big(2\nu q_x^2 + q_y^2\big)$$

$$- 4(1-\nu)\frac{q_xq_yq_x'q_y'}{q^3q'}[q_y(q_y - q_y') - q_x(q_x - q_x')]\bigg\}\hat{h}(\mathbf{q}')\hat{h}(\mathbf{q} - \mathbf{q}'),$$
(A3)

$$\varepsilon^2\hat{\sigma}_{zz}^{(2)f}(\mathbf{q}) = \frac{E\epsilon_m}{(1-\nu)}(3 - 2\nu)\sum_{\mathbf{q}'}[q_x'(q_x - q_x') + q_y'(q_y - q_y')]\hat{h}(\mathbf{q}')\hat{h}(\mathbf{q} - \mathbf{q}'),$$
(A4)

$$\varepsilon^2\hat{\sigma}_{xy}^{(2)f}(\mathbf{q}) = E\epsilon_m\sum_{\mathbf{q}'}\left\{-4\frac{q_xq_y}{q'q^3}\big[\big(q_x(q_x - q_x')\big(q_x'^2 + \nu q_y'^2\big) + q_y(q_y - q_y')\big(q_y'^2 + \nu q_x'^2\big)\big)\right.$$

$$+ (1-\nu)q_x'q_y'\big(q_x(q_y - q_y') + q_y(q_x - q_x')\big)\big] + \frac{(1-2\nu)}{(1-\nu)}\frac{q_xq_y}{q^2}[q_x'(q_x - q_x') + q_y'(q_y - q_y')]$$

$$- \frac{4}{(1-\nu)}\frac{q_y^2}{q^3q'}\big[q_y(q_x - q_x')\big(q_x'^2 + \nu q_y'^2\big) - q_x(q_y - q_y')\big(q_y'^2 + \nu q_x'^2\big)$$

$$+ (1-\nu)q_x'q_y'\big(q_y(q_y - q_y') - q_x(q_x - q_x')\big)\big]\bigg\}\hat{h}(\mathbf{q}')\hat{h}(\mathbf{q} - \mathbf{q}'),$$
(A5)

$$\varepsilon^2 \hat{\sigma}_{xz}^{(2)f}(\mathbf{q}) = \frac{2E\epsilon_m}{1-\nu} \sum_{\mathbf{q}'} i \frac{q_x}{q^2 q'} \bigg\{ q_x(q_x - q_x')(q_x'^2 + \nu q_y'^2) + q_y(q_y - q_y')(q_y'^2 + \nu q_x'^2)$$

$$+ (1-\nu)q_x'q_y'[q_x(q_y - q_y') + q_y(q_x - q_x')] - \frac{q_y^2}{q_x}\big[(q_x - q_x')(q_x'^2 + \nu q_y'^2) + (1-\nu)(q_y - q_y')q_x'q_y'\big]$$

$$+ (1-\nu)q_y(q_x - q_x')q_x'q_y' + q_y(q_y - q_y')(q_y'^2 + \nu q_x'^2) \bigg\} \hat{h}(\mathbf{q}')\hat{h}(\mathbf{q} - \mathbf{q}'), \tag{A6}$$

$$\varepsilon^2 \hat{\sigma}_{yz}^{(2)f}(\mathbf{q}) = \frac{2E\epsilon_m}{1-\nu} \sum_{\mathbf{q}'} i \frac{q_y}{q^2 q'} \bigg\{ q_x(q_x - q_x')(q_x'^2 + \nu q_y'^2) + q_y(q_y - q_y')(q_y'^2 + \nu q_x'^2)$$

$$+ (1-\nu)q_x'q_y'[q_x(q_y - q_y') + q_y(q_x - q_x')] - \frac{q_x^2}{q_y}\big[(q_y - q_y')(q_y'^2 + \nu q_x'^2) + (1-\nu)(q_x - q_x')q_x'q_y'\big]$$

$$+ (1-\nu)q_x(q_y - q_y')q_x'q_y' + q_x(q_x - q_x')(q_x'^2 + \nu q_y'^2) \bigg\} \hat{h}(\mathbf{q}')\hat{h}(\mathbf{q} - \mathbf{q}'). \tag{A7}$$

[1] J. Stangl, V. Holy, and G. Bauer, Rev. Mod. Phys. **76**, 725 (2004).

[2] S. Kiravittaya, A. Rastelli, and O. G. Schmidt, Rep. Prog. Phys. **72**, 046502 (2009).

[3] I. Berbezier and A. Ronda, Surf. Sci. Rep. **64**, 47 (2009).

[4] R. J. Asaro and W. A. Tiller, Metall. Trans. **3**, 1789 (1972); M. A. Grinfeld, Sov. Phys. Dokl. **31**, 831 (1986) [Dokl. Akad. Nauk SSSR **290**, 1358 (1986)].

[5] D. J. Srolovitz, Acta Metall. **37**, 621 (1989).

[6] B. J. Spencer, P. W. Voorhees, and S. H. Davis, Phys. Rev. Lett. **67**, 3696 (1991); J. Appl. Phys. **73**, 4955 (1993).

[7] P. Sutter and M. G. Lagally, Phys. Rev. Lett. **84**, 4637 (2000).

[8] R. M. Tromp, F. M. Ross, and M. C. Reuter, Phys. Rev. Lett. **84**, 4641 (2000).

[9] J. Tersoff, B. J. Spencer, A. Rastelli, and H. von Känel, Phys. Rev. Lett. **89**, 196104 (2002).

[10] J. E. Guyer and P. W. Voorhees, Phys. Rev. Lett. **74**, 4031 (1995).

[11] B. J. Spencer, P. W. Voorhees, and J. Tersoff, Phys. Rev. B **64**, 235318 (2001).

[12] Z.-F. Huang and R. C. Desai, Phys. Rev. B **65**, 205419 (2002); **65**, 195421 (2002).

[13] R. C. Desai, H. K. Kim, A. Chatterji, D. Ngai, S. Chen, and N. Yang, Phys. Rev. B **81**, 235301 (2010).

[14] L. E. Shilkrot, D. J. Srolovitz, and J. Tersoff, Phys. Rev. B **62**, 8397 (2000); **67**, 249901(E) (2003).

[15] Z.-F. Huang and R. C. Desai, Phys. Rev. B **67**, 075416 (2003); Z.-F. Huang, D. Kandel, and R. C. Desai, Appl. Phys. Lett. **82**, 4705 (2003).

[16] F. M. Ross, J. Tersoff, and R. M. Tromp, Phys. Rev. Lett. **80**, 984 (1998).

[17] G. Medeiros-Ribeiro, T. I. Kamins, D. A. A. Ohlberg, and R. S. Williams, Phys. Rev. B **58**, 3533 (1998).

[18] A. Rastelli, M. Stoffel, J. Tersoff, G. S. Kar, and O. G. Schmidt, Phys. Rev. Lett. **95**, 026103 (2005).

[19] M. R. McKay, J. A. Venables, and J. Drucker, Phys. Rev. Lett. **101**, 216104 (2008).

[20] J. A. Floro, M. B. Sinclair, E. Chason, L. B. Freund, R. D. Twesten, R. Q. Hwang, and G. A. Lucadamo, Phys. Rev. Lett. **84**, 701 (2000).

[21] T. J. Krzyzewski and T. S. Jones, J. Appl. Phys. **96**, 668 (2004).

[22] W. Dorsch, H. P. Strunk, H. Wawra, G. Wagner, J. Groenen, and R. Carles, Appl. Phys. Lett. **72**, 179 (1998).

[23] W. H. Yang and D. J. Srolovitz, Phys. Rev. Lett. **71**, 1593 (1993).

[24] B. J. Spencer, S. H. Davis, and P. W. Voorhees, Phys. Rev. B **47**, 9760 (1993).

[25] B. J. Spencer and D. I. Meiron, Acta Metall. Mater. **42**, 3629 (1994).

[26] C.-H. Chiu, Appl. Phys. Lett. **75**, 3473 (1999); C.-H. Chiu and Z. Huang, J. Appl. Phys. **101**, 113540 (2007).

[27] F. Liu, A. H. Li, and M. G. Lagally, Phys. Rev. Lett. **87**, 126103 (2001).

[28] Y. Xiang and W. E, J. Appl. Phys. **91**, 9414 (2002).

[29] P. Liu, Y. W. Zhang, and C. Lu, Phys. Rev. B **68**, 035402 (2003).

[30] A. A. Golovin, S. H. Davis, and P. W. Voorhees, Phys. Rev. E **68**, 056203 (2003).

[31] W. T. Tekalign and B. J. Spencer, J. Appl. Phys. **96**, 5505 (2004); **102**, 073503 (2007).

[32] H. R. Eisenberg and D. Kandel, Phys. Rev. B **71**, 115423 (2005).

[33] Y. Pang and R. Huang, Phys. Rev. B **74**, 075413 (2006).

[34] M. S. Levine, A. A. Golovin, S. H. Davis, and P. W. Voorhees, Phys. Rev. B **75**, 205312 (2007).

[35] J.-N. Aqua, T. Frisch, and A. Verga, Phys. Rev. B **76**, 165319 (2007); Phys. Rev. E **81**, 021605 (2010).

[36] J. Müller and M. Grant, Phys. Rev. Lett. **82**, 1736 (1999).

[37] K. Kassner, C. Misbah, J. Müller, J. Kappey, and P. Kohlert, Phys. Rev. E **63**, 036117 (2001).

[38] G. Nandipati and J. G. Amar, Phys. Rev. B **73**, 045409 (2006).

[39] T. P. Schulze and P. Smereka, J. Mech. Phys. Solids **57**, 521 (2009).

[40] X. B. Niu, G. B. Stringfellow, and F. Liu, Phys. Rev. Lett. **107**, 076101 (2011).

[41] K. R. Elder, M. Katakowski, M. Haataja, and M. Grant, Phys. Rev. Lett. **88**, 245701 (2002).

[42] Z.-F. Huang and K. R. Elder, Phys. Rev. Lett. **101**, 158701 (2008); Phys. Rev. B **81**, 165421 (2010).

[43] K.-A. Wu and P. W. Voorhees, Phys. Rev. B **80**, 125408 (2009).

[44] K. R. Elder, Z.-F. Huang, and N. Provatas, Phys. Rev. E **81**, 011602 (2010); K. R. Elder and Z.-F. Huang, J. Phys.: Condens. Matter **22**, 364103 (2010); Z.-F. Huang, K. R. Elder, and N. Provatas, Phys. Rev. E **82**, 021605 (2010).

[45] J.-N. Aqua and T. Frisch, Phys. Rev. B **82**, 085322 (2010).

[46] M. C. Cross, D. I. Meiron, and Y. Tu, Chaos **4**, 607 (1994).

[47] C. Sagui and R. C. Desai, Phys. Rev. E **49**, 2225 (1994).